NANO LETTERS

pubs.acs.org/NanoLett Letter

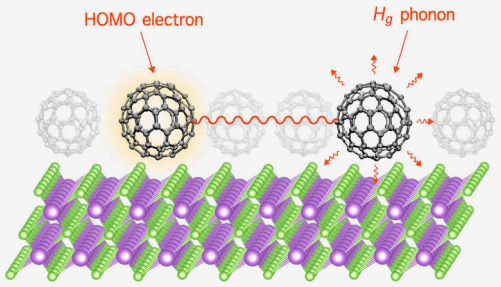
Layer-Controlled Intermolecular Coupling and Many-Body Effects in C_{60} Films

Hai-Lan Luo, Weitang Li, Luca Moreschini, Jonathan Denlinger, Zhigang Shuai, Claudia Ojeda-Aristizabal, and Alessandra Lanzara*

Cite This: *Nano Lett.* 2026, 26, 12259−12267 Read Online

ACCESS | Metrics & More | Article Recommendations | Supporting Information

ABSTRACT: Crystalline C_{60} is a molecular solid whose electronic properties emerge from the interplay of intermolecular hopping, electron correlations, and electron−vibration coupling. Unlike moiré van der Waals heterostructures, where the interaction strength is commonly tuned by twist angle, molecular materials offer a complementary route in which the layer number, molecular orientation, and substrate registry provide experimentally accessible control parameters. Here we present a systematic thickness-dependent angle-resolved photoemission study of C_{60} films, spanning the monolayer to the bulk limit. The HOMO-derived band exhibits a nonmonotonic evolution: the intermediate-thickness film shows a larger bandwidth, a reduced effective mass, and a pronounced gap-like and sub-band features. The experimental trends, together with Holstein-model simulations, point to strengthened effective intermolecular electronic coupling and enhanced electron−phonon-induced spectral renormalization in the intermediate-thickness regime. These results identify a dimensional crossover in C_{60} films and establish the layer number as an effective knob for engineering electronic structure and many-body interactions in molecular thin films.



KEYWORDS: *C_{60} molecular films, angle-resolved photoemission spectroscopy, intermolecular coupling, electron−phonon coupling*

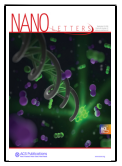
The ability to tune the electronic structure and many-body interactions is central to the design of quantum materials.[1,2] In van der Waals heterostructures, moiré superlattices have demonstrated how structural control can reshape the bandwidth, symmetry, and interaction strength.[3,4] Molecular solids, assemblies of molecules bound by van der Waals interactions, offer a complementary platform. Unlike conventional atomic crystals, they possess internal rotational and orientational degrees of freedom that directly influence intermolecular overlap and electronic coupling.[5−8] Their electronic properties are therefore governed not only by lattice symmetry but also by intermolecular overlap, molecular orientation, and coupling to intramolecular vibrations. In molecular thin films, these structural degrees of freedom can be accessed through experimentally tunable parameters such as the layer number, molecular orientation, and substrate registry, providing flexible knobs for tuning the electronic structure and many-body interactions.[5,9,10]

Among molecular crystals, crystalline C_{60} stands out as a promising system, enabling diverse device functionalities[11−16] and allowing controlled studies of collective and correlated quantum phenomena.[5,17−21] Its electronic properties are intimately governed by competing interactions, including intermolecular hopping, electron−electron correlation, and electron−vibration coupling.[22−25] Disentangling these microscopic ingredients is therefore essential for understanding and ultimately controlling the emergent properties.

A natural route toward this goal is to tune these interactions through experimentally accessible structural parameters. In layered van der Waals materials, the layer number has proven to be a powerful control parameter, revealing how interlayer coupling and symmetry shape electronic states.[26−33] This concept naturally extends to crystalline C_{60} films, where changing the layer number can modify the dimensionality, intermolecular coupling, orientational order, and substrate-induced effects. Indeed, a variety of emergent states have been observed in C_{60}-based platforms across different dimensional realizations, such as superconductivity and magnetism in bulk compounds,[19,20] unconventional electronic and orientational phases in thin films,[9,10,22,25,34,35] and quantum transport in single-molecule devices.[36] However, a systematic understanding of how dimensionality influences the microscopic electronic structure and many-body effects in pristine, well-controlled C_{60} films remains lacking.

Building on established layer-by-layer growth of C_{60} films and the ability of angle-resolved photoemission spectroscopy (ARPES) to resolve their dispersive band structure,[37,38] we

Received: May 10, 2026
Revised: August 23, 2026
Accepted: August 27, 2026
Published: September 4, 2026



ACS Publications © 2026 American Chemical Society

https://doi.org/10.1021/acs.nanolett.6c02272
Nano Lett. 2026, 26, 12259−12267

Downloaded from pubs.acs.org/naletd/article-pdf/26/37/12259/6394856/acs.nanolett.6c02272.pdf by CHINESE UNIV OF HONG KONG SHENZHEN user on 02 November 2026

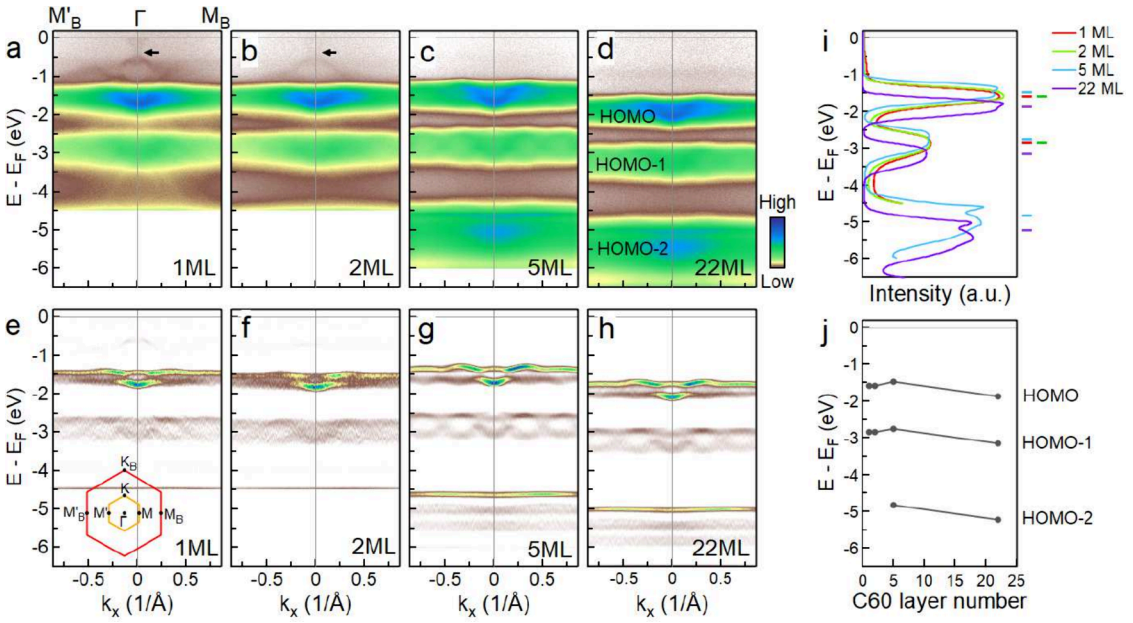


Figure 1. Thickness-dependent electronic structures of C_{60} films on a Bi_2Se_3 substrate. ARPES band structures of C_{60} films with thicknesses of 1 ML (a), 2 ML (b), 5 ML (c), and 22 ML (d), measured along the $M_B'-\Gamma-M_B$ high-symmetry direction. Bands originating from the Bi_2Se_3 substrate are indicated by arrows in parts a and b. (e–h) Second-derivative images with respect to energy, derived from parts a–d. The Brillouin zones of C_{60} and Bi_2Se_3 are outlined in yellow and red, respectively, in the inset of part e. (i) EDCs integrated over the full $M_B'-\Gamma-M_B$ momentum range for all four thicknesses. The colored bars on the right indicate the centroid energy of each band manifold. (j) Thickness dependence of the centroid energies of each band manifold, extracted from the EDCs.

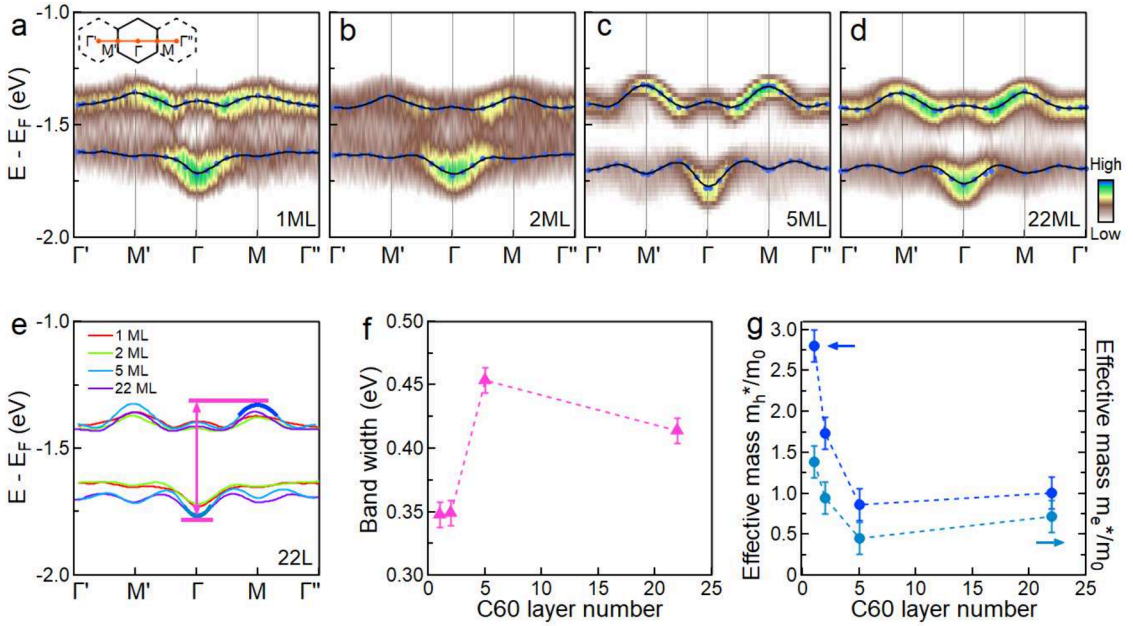


Figure 2. Thickness-dependent band dispersion and effective mass of the HOMO band. Second-derivative ARPES spectra of the HOMO band along the M′–Γ–M high-symmetry direction for C_{60} films with thicknesses of 1 ML (a), 2 ML (b), 5 ML (c), and 22 ML (d). Blue dots indicate extracted peak positions of the dominant HOMO-derived dispersive spectral envelope, and black curves represent fits to these features. (e) Fitted dispersions for all thicknesses overlaid for comparison. Blue curves show parabolic fits around the band top at M and the band bottom at Γ for the 22 ML film. The magenta arrow indicates the HOMO bandwidth (W) of the dominant HOMO-derived dispersive spectral envelope, defined as the energy difference between the fitted band maximum at M/M′ and the fitted band minimum at Γ. (f) Thickness dependence of W. (g) Effective hole masses (m_h^*) at M/M′ and electron masses (m_e^*) at Γ, extracted from local parabolic fits near the corresponding band extrema.

systematically investigate the thickness-dependent electronic structure of C_{60} films over a wide thickness range, from a monolayer (1 ML) to a bulk-like thickness of 22 layers (22 ML). By tracking the evolution of the highest occupied molecular orbital (HOMO) and its adjacent HOMO−1 band, we extract layer-dependent changes in the bandwidth, dispersion, and effective mass. A pronounced crossover emerges in the intermediate-thickness regime, where the HOMO bandwidth is the largest among the measured thicknesses, consistent with strengthened effective intermo-

https://doi.org/10.1021/acs.nanolett.6c02272
Nano Lett. 2026, 26, 12259−12267

Downloaded from pubs.acs.org/naletd/article-pdf/26/37/12259/6394856/acs.nanolett.6c02272.pdf by CHINESE UNIV OF HONG KONG SHENZHEN user on 02 November 2026

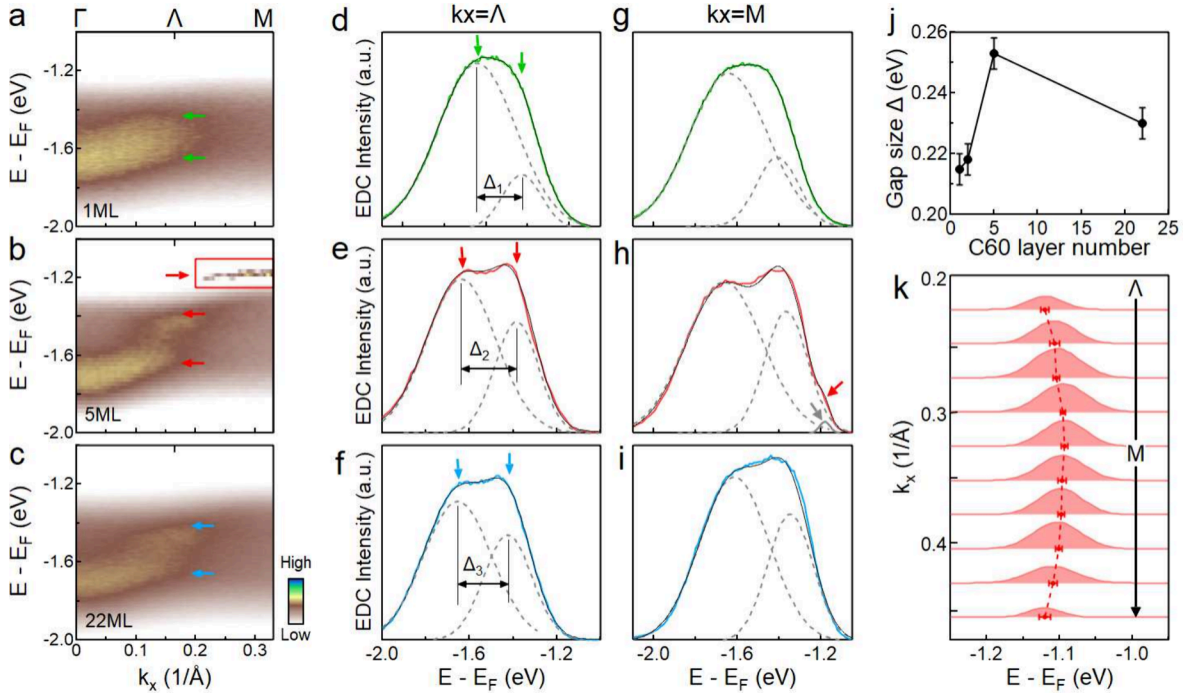


Figure 3. Thickness-dependent gap-like and sub-band features. Raw ARPES intensity maps of the HOMO band dispersion for 1 ML (a), 5 ML (b), and 22 ML (c) C_{60} films. The Λ point denotes the midpoint between Γ and M. The inset in part b shows the second-derivative image, highlighting the sub-band feature in the 5 ML film; the corresponding raw-intensity evidence is provided in Figure S3. EDCs at the Λ point for C_{60} films with thicknesses of 1 ML (d), 5 ML (e), and 22 ML (f), showing gap-like structures. Spectra are fitted with two Gaussian components, as shown by gray dashed curves. EDCs at the M point for C_{60} films with thicknesses of 1 ML (g), 5 ML (h), and 22 ML (i). A shoulder feature is observed in the 5 ML film and fitted with an additional Gaussian component, as indicated by arrows in part h. (j) Extracted gap size at the Λ point as a function of the thickness. (k) Momentum dependence of the sub-band feature in the 5 ML film along the Λ−M direction, showing a hole-like dispersion.

lecular electronic coupling. At the same thickness (5 ML), gap-like features that are present across all thicknesses become most prominent, and a distinct sub-band appears within the HOMO. Together with Holstein-model simulations, these observations identify an intermediate-thickness regime in which intermolecular hopping and electron−vibration coupling are simultaneously enhanced, establishing the layer number as an effective knob for tuning many-body interactions in molecular thin films.

Taking advantage of the structural adaptability of C_{60} molecules to various substrates, we grow C_{60} thin films crystallizing in the $Pa\bar{3}$ structure, with thickness ranging from 1 ML to the bulk-like regime, by molecular beam epitaxy (MBE) on the (111) surface of the topological insulator Bi_2Se_3. Due to the 3.4% uniaxial compressive strain imposed by lattice mismatch, the rotational disorder of C_{60} molecules is suppressed, facilitating the resolution of dispersive molecular orbitals in ARPES.[37] The suppression of rotational disorder stabilizes a well-defined intermolecular overlap, enabling the thickness-dependent evolution of electronic coupling observed here. This controlled platform enables a systematic investigation of how the layer number modulates the intermolecular coupling and electronic structure. Figure 1 presents the evolution of the electronic structure of C_{60} as a function of the film thickness along the M_B'−Γ−M_B high-symmetry direction. We focus on the two uppermost valence bands, which are mainly derived from the HOMO and the next-highest occupied molecular orbital (HOMO−1). The highly dispersive character of these bands is more clearly visualized in the second-derivative images (Figure 1e−h), with the band extrema located at Γ, M, and M′.

Residual band features from the Bi_2Se_3 substrate are also visible in the thinner films (1 and 2 ML), as indicated by arrows in Figure 1a,b, but disappear in the thicker ones (5 and 22 ML; Figure 1c,d) because of the surface sensitivity of ARPES. This evolution reflects the progressive decoupling of the C_{60} electronic states from the substrate with increasing thickness.

To further examine the thickness dependence of the valence states, Figure 1i displays the integrated energy distribution curves (EDCs) for the four film thicknesses. The full width at half-maximum of the HOMO and HOMO−1 peaks remains nearly constant at 500 and 670 meV, respectively, across all thicknesses. This indicates that the overall quasiparticle lifetime and disorder broadening remain comparable across the series. In addition, the centroid energies of all bands exhibit a nonmonotonic dependence on the film thickness (Figure 1j). While their positions remain nearly constant in the 1−5 ML regime, a pronounced downward shift of approximately 300 meV is observed in the 22 ML film. This shift likely reflects charging effects associated with the low conductivity and wide band gap of thick C_{60} layers.

A quantitative analysis of the band dispersion is presented in Figure 2. Panels a−d show enlarged second-derivative images of the HOMO band along the M′−Γ−M high-symmetry direction for C_{60} films with four thicknesses. Two dispersive branches are clearly resolved by fitting the data (black curves in Figure 2a−d): an upper branch with its band maximum at the M/M′ points and a lower branch with its minimum at Γ. The fitted dispersions for all thicknesses are overlaid in Figure 2e for comparison. From these results, we extract the HOMO bandwidth (W) and effective masses (m^*) as a function of the

https://doi.org/10.1021/acs.nanolett.6c02272
Nano Lett. 2026, 26, 12259−12267

Downloaded from pubs.acs.org/naletd/article-pdf/26/37/12259/6394856/acs.nanolett.6c02272.pdf by CHINESE UNIV OF HONG KONG SHENZHEN user on 02 November 2026

film thickness, as plotted in parts f and g of Figure 2, respectively. The HOMO-derived valence states are associated with the 5-fold-degenerate molecular h_u HOMO manifold of C_{60}, which can give rise to multiple HOMO-derived bands in the crystalline film.[39] Given the multiband nature of this manifold and the matrix-element sensitivity of C_{60} photoemission,[40] a unique sub-band-by-sub-band assignment is not feasible from the present ARPES data alone. We therefore define the HOMO bandwidth W as the experimentally extracted energy range of the dominant HOMO-derived dispersive spectral envelope along the measured M′−Γ−M direction rather than as the bandwidth of a single isolated tight-binding band.

The extracted HOMO bandwidth and effective masses reveal a clear dependence on the film thickness. The HOMO bandwidth W is approximately 350 meV in the 1 and 2 ML C_{60} films, increases to ∼450 meV in the 5 ML film, and then decreases by ∼40 meV in the much thicker 22 ML film (Figure 2f). In molecular solids, the HOMO bandwidth is strongly influenced by intermolecular orbital overlap and transfer integrals. However, because the HOMO-derived valence states of crystalline C_{60} form a multiband manifold, the extracted W should not be interpreted as a quantitative measure of a unique microscopic hopping parameter. This nonmonotonic behavior indicates that the layer number acts as an effective tuning parameter for intermolecular hopping, with a maximum coupling reached at intermediate thickness. A similar thickness dependence is observed in the local band curvature. By performing parabolic fits to the HOMO band near the band top at M and the band bottom at Γ, we extract the effective masses of holes (m_h^*) and electrons (m_e^*) as a function of the layer number (Figure 2g). Both m_h^* and m_e^* reach their minimum values at 5 ML and increase significantly toward the monolayer limit. The reduced effective mass in the 5 ML film is consistent with a more dispersive HOMO-derived band and the largest bandwidth among the measured thicknesses. We also note that although the 1 and 2 ML films exhibit comparable HOMO bandwidths, their extracted local effective masses differ by approximately a factor of 2. This difference is not unexpected because the HOMO-derived states form a multiband manifold rather than a simple single-band system governed by a single hopping parameter. Therefore, the HOMO bandwidth and local effective mass should be regarded as complementary empirical indicators of the HOMO-derived dispersion rather than as two equivalent measures of a unique microscopic hopping parameter. Together, these results identify an intermediate-thickness regime characterized by a larger measured HOMO bandwidth and reduced local effective masses, consistent with strengthened effective intermolecular electronic coupling.

Notably, the nonmonotonic evolution of the bandwidth and effective mass is accompanied by other thickness-dependent spectral reconstructions: a gap-like feature appears at the Λ point in all films but is most pronounced at 5 ML, where a distinct sub-band feature also emerges. The coincidence of these features with the maximum bandwidth suggests a common underlying interaction driving both band dispersion and spectral renormalization. Parts a−c of Figure 3 present the raw data of the HOMO band of representative 1, 5, and 22 ML films; the 2 ML data are omitted because it closely resemble the 1 ML data.

To quantify the thickness-dependent evolution of the gap-like feature, we compare the EDCs at the Λ point (Figure 3d−f). Each EDC can be well reproduced by two Gaussian components (gray dashed curves), clearly indicating the presence of a gap-like feature. The extracted gap sizes, Δ_1, Δ_2, and Δ_3, for the 1, 5, and 22 ML films, respectively, evolve nonmonotonically with thickness and peak at 5 ML, as summarized in Figure 3j. This behavior mirrors the evolution of the bandwidth, suggesting a correlation between effective intermolecular coupling and the strength of the spectral gap.

In addition to the gap-like feature at Λ, the EDCs at the M point also exhibit a notable thickness dependence. As shown in Figure 3g−i, a pronounced shoulder near the band top is observed in the 5 ML C_{60} film and is absent in the 1 and 22 ML films. To quantify this feature, we fit the EDCs at M. The spectra of the 1 and 22 ML films (Figure 3g,i) are well described by two Gaussian components (gray dashed curves), yielding excellent overall fits (black curves). In contrast, the EDC of the 5 ML film (Figure 3h) cannot be satisfactorily described using only two Gaussian components; a third component (gray arrow) is required to account for the shoulder on the low-binding-energy side (red arrow). This additional spectral component indicates the emergence of a new electronic feature that is stabilized only at intermediate thickness.

Momentum-resolved analysis of this sub-band (Figure 3k) reveals a hole-like dispersion with a band maximum at M, closely resembling the main HOMO band. Its spectral weight, however, is highly localized in momentum space and decays rapidly beyond $k_M \pm 0.12$ Å^{-1}. A parabolic fit to this sub-band yields an energy separation of ∼180 meV from the HOMO maximum. The similarity in dispersion together with the fixed energy offset suggests that this feature does not originate from a distinct band but rather from a many-body renormalization of the primary electronic state.

The gap-like feature and sub-band formation are common spectroscopic signatures of electron−phonon coupling, as reported across semiconductors,[41,42] superconductors,[43] and organic molecular materials.[44−47] In weakly coupled molecular films, where the bandwidth (W) is comparable to the intramolecular vibrational energy (Ω), electron−vibration coupling can produce shake-off replica bands below the main band.[45] The energy separation between the main band and its replicas is determined by Ω, while their relative intensities reflect the coupling strength. In molecular crystals with stronger intermolecular coupling ($W > \Omega$), electron−phonon interactions can give rise to more complex spectral features. Specifically, theoretical studies have predicted that the HOMO band can split into a series of sub-bands separated by gaps.[44,46,47] These considerations suggest that the observed thickness-dependent spectral features may originate from a coupling between the electronic states and intramolecular vibrational modes.

To test this hypothesis, we identify the phonon modes most likely to contribute to the coupling. In typical systems, the energy separation between the main band and its replica is set by the energy of the coupled phonon mode.[41−43,45] In the 5 ML C_{60} film, the observed energy separation of 180 meV closely matches two high-frequency intramolecular phonon modes, $H_g(7)$ and $H_g(8)$, with vibrational wavenumbers of 1443 cm^{-1} (178 meV) and 1607 cm^{-1} (198 meV), respectively.[48,49] Moreover, among all H_g phonons in C_{60}, these two modes exhibit the strongest electron−phonon coupling via the Jahn−Teller effect.[49] The quantitative agreement between the sub-band separation and the vibra-

Downloaded from pubs.acs.org/naletd/article-pdf/26/37/12259/6394856/acs.nanolett.6c02272.pdf by CHINESE UNIV OF HONG KONG SHENZHEN user on 02 November 2026

https://doi.org/10.1021/acs.nanolett.6c02272
Nano Lett. 2026, 26, 12259−12267

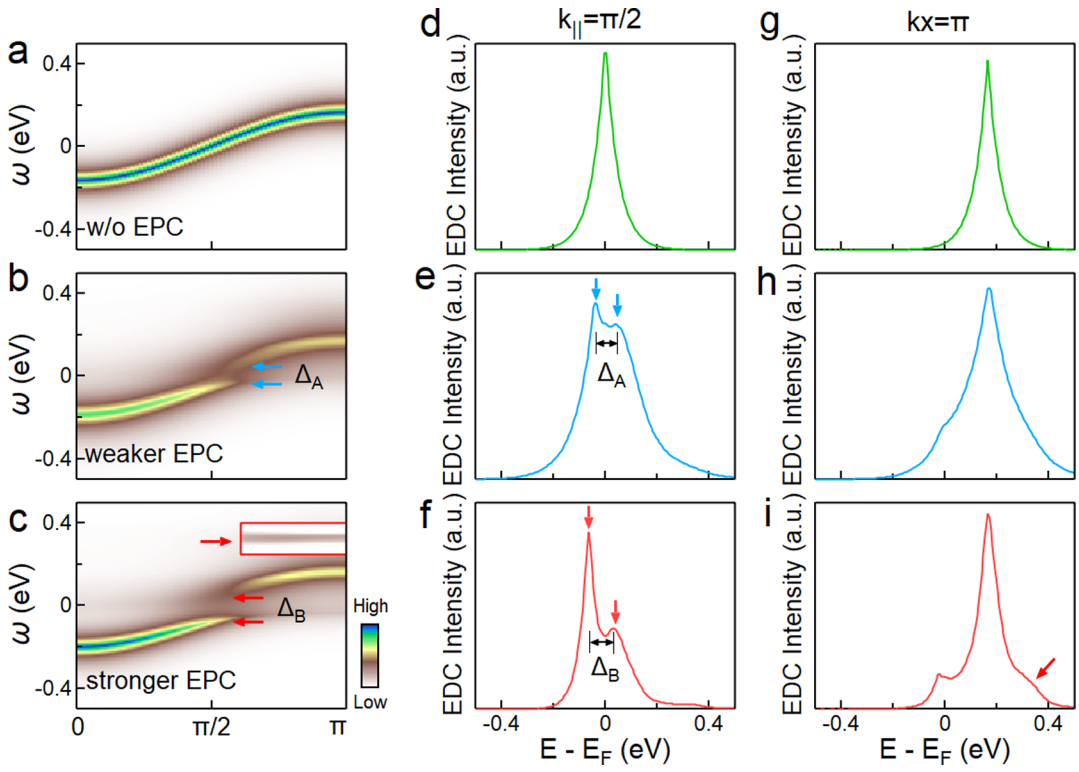


Figure 4. Simulated spectral functions with varying electron−phonon coupling strength. Simulated single-particle spectral functions of the HOMO band based on a Holstein model with coupling to the $H_g(7)$ (1443 cm^{-1}) and $H_g(8)$ (1607 cm^{-1}) intramolecular phonon modes. The mode-resolved reorganization energy ($g_m{}^2\omega_m$) for each of these two modes is set to 0 meV in part a, 20 meV in part b, and 30 meV in part c, corresponding to the no-coupling, intermediate-coupling, and stronger-coupling cases, respectively. Arrows indicate gap-like features and sub-band formation. (d−f) Corresponding EDCs at $k_{||} = \pi/2$ for the three electron−phonon coupling strengths, showing the evolution from a single peak to a split structure with increasing coupling strength. (g−i) Corresponding EDCs at $k_{||} = \pi$ for the same three electron−phonon coupling strengths, showing the emergence of a sub-band feature at stronger coupling.

tional energies provides strong evidence that these modes dominate the observed spectral renormalization. We therefore incorporate $H_g(7)$ and $H_g(8)$ into our simulations.

We emphasize that this Holstein-model calculation is not intended as a full multiband fit to the experimental HOMO manifold. Instead, it provides a minimal phenomenological description to test whether coupling to high-frequency intramolecular modes can generate gap-like features and sub-band spectral weight comparable to those observed experimentally. To enable a comparison with our experimental data, we calculate the single-particle spectral function using the Holstein model, both without and with electron-vibration coupling. Figure 4a shows the simulated spectral function described by a tight-binding dispersion, $\omega(k_{||}) = \omega_0 - 2V\cos(ak_{||})$, with a Lorentzian broadening of 50 meV. Here, ω_0 is set to 0 meV as the energy reference, and the effective hopping parameter V = 87.5 meV is chosen to reproduce the approximate energy scale of the monolayer HOMO bandwidth W (Figure 2). The simulated EDCs at $k_{||} = \pi/2$ and π, taken from Figure 4a, both display single-peak structures (Figures 4d,g), as expected in the absence of electron−phonon coupling. This baseline calculation establishes that the additional spectral features observed experimentally do not arise from the underlying band structure alone.

Figure 4b shows the simulated spectral function in the presence of electron−phonon interactions. The $H_g(7)$ and $H_g(8)$ modes are included with equal coupling strengths, corresponding to a reorganization energy of 20 meV (see the Supporting Information). The resulting spectrum exhibits a gap (Δ_A) at $k_{||} = \pi/2$ but no sub-band feature near π, as confirmed by the corresponding EDCs obtained at $\pi/2$ (Figure 4e) and π (Figure 4h). This intermediate-coupling regime reproduces the partial spectral renormalization observed experimentally, characterized by the presence of a gap without a well-defined sub-band. In particular, it captures the behavior of the thicker (22 ML) film, where spectral reconstruction is present but remains limited in strength.

In contrast, Figure 4c presents the spectral function calculated with stronger electron−phonon interactions. Here, both $H_g(7)$ and $H_g(8)$ modes are assigned larger coupling strengths, corresponding to a reorganization energy of 30 meV. A clear gap opens near $k_{||} = \pi/2$, and a sub-band emerges above the HOMO top at π, as highlighted by the second-derivative image. Quantitatively, the EDC at $\pi/2$ in Figure 4f clearly displays a distinct two-peak structure, with a gap size Δ_B larger than Δ_A, reflecting the effect of enhanced electron−phonon coupling. Meanwhile, the EDC at π in Figure 4i shows a shoulder feature associated with the sub-band above the HOMO top, as indicated by an arrow. Importantly, the energy separation between the sub-band and the HOMO top agrees well with the experimental observations and is consistent with the characteristic vibrational energy scale identified experimentally. This strong-coupling regime simultaneously captures both the enlarged gap and the emergence of the sub-band, providing a unified description of the spectral features observed at intermediate thickness. In particular, it reproduces the behavior of the 5 ML film, where spectral renormalization is most pronounced within the measured thickness series,

https://doi.org/10.1021/acs.nanolett.6c02272
Nano Lett. 2026, 26, 12259−12267

Downloaded from pubs.acs.org/naletd/article-pdf/26/37/12259/6839486/acs.nanolett.6c02272.pdf by CHINESE UNIV OF HONG KONG SHENZHEN user on 02 November 2026

linking the observed electronic reconstruction to an enhanced electron−phonon interaction strength. Notably, our simulations show that the number and spacing of phonon-induced gap-like features are governed primarily by the energy scale of the dominant phonon modes, with high-frequency $H_g(7)$- and $H_g(8)$-dominated coupling naturally yielding a single prominent gap opening rather than multiple closely spaced gaps, as discussed in the Supplementary Note and shown in Figure S2.

The thickness-dependent evolution of the HOMO bandwidth and local effective mass in C_{60} films suggests a strengthened effective intermolecular electronic coupling in the intermediate-thickness regime. Rather than evolving monotonically, these quantities reach extrema in the intermediate-thickness regime, followed by possible saturation or weakening in thicker films, identifying the layer number as an effective control parameter for tuning electronic dispersion in molecular solids. Strikingly, this trend closely parallels the evolution of the gap-like feature and the emergence of the sub-band, which are also most pronounced at the same thickness. Although charging may affect the precise quantitative value extracted for the 22 ML bandwidth, the overall conclusion does not rely on this quantity alone. The 5 ML film, as the measured representative of the intermediate-thickness regime, simultaneously exhibits enhanced HOMO-derived dispersion, reduced local effective masses, the most pronounced gap-like feature, and the clearest sub-band spectral weight. It is unlikely that charging alone would produce such a correlated evolution across several independent observables. Therefore, while the precise quantitative values extracted for the 22 ML film should be interpreted with caution, the overall trend toward strengthened effective intermolecular electronic coupling and enhanced electron−phonon-induced spectral renormalization in the intermediate-thickness regime remains robust. The energy separation between the main HOMO band and the sub-band in the 5 ML film hints at the involvement of the high-frequency intramolecular vibrational modes, $H_g(7)$ and $H_g(8)$. By incorporating these modes into a Holstein model, we reproduce the experimentally observed thickness dependence of both the gap-like feature and the sub-band under varying electron−phonon coupling strengths. Taken together, these results demonstrate that the film thickness simultaneously tunes both intermolecular and electron−phonon coupling, linking band dispersion and many-body renormalization through a single experimentally accessible control parameter.

To understand the origin of this crossover, we examine the role of strain. A uniaxial compressive strain of 3.4% has been reported for C_{60} films grown on Bi_2Se_3,[37] and this strain is expected to relax as the film thickness increases. Compressive strain reduces the intermolecular spacing and enhances the wave function overlap, thereby naturally accounting for the stronger intermolecular hopping in the 5 ML film than in the 22 ML film.[50−52] However, strain alone cannot explain the weaker coupling in 1−2 ML films, which are expected to experience compressive strain no smaller than that in the top layer of the 5 ML film. A likely origin of this behavior is static disorder from the Bi_2Se_3 substrate. In this scenario, the bottom one or two C_{60} layers are more susceptible to electrostatic potential fluctuations caused by surface defects, such as Se or Bi vacancies,[53] which can generate trap states and hinder coherent intermolecular hopping.[54] The observed crossover can therefore be understood as the result of competing effects: substrate-induced disorder suppresses coherence in the ultrathin limit, while strain relaxation reduces intermolecular overlap in thicker films. In addition to these effects, thickness-dependent changes in screening and molecular orientation may also contribute to the observed HOMO bandwidth and local band curvature. The intermediate-thickness regime balances these effects, leading to enhanced electronic coherence and interaction strength.

The origin of the thickness dependence of electron−phonon coupling likely involves multiple factors. One plausible contribution is strain, which has been shown to modulate the electron−phonon coupling strength in some quantum materials.[55] Whether this mechanism also applies to C_{60} films remains an open question. A second possibility is a thickness-dependent interlayer effect. In layered systems with strong interlayer coupling, the film thickness can directly influence the electron−phonon coupling strength;[56] although C_{60} is generally regarded as a molecular solid with weak interlayer van der Waals interactions, related effects cannot be ruled out a priori. Charge transfer from the substrate may also play a role by enhancing interlayer effects through induced dipoles,[57] although direct evidence for such a transfer in C_{60}/Bi_2Se_3 under our experimental conditions is currently lacking.[58] Taken together, these considerations suggest that the thickness dependence of the electron−phonon coupling arises from an interplay of strain, disorder, and interlayer effects. While the relative contributions of these mechanisms remain to be fully resolved, our results demonstrate that the layer number provides an effective experimental knob for tuning electron−phonon interactions in molecular thin films.

In particular, the simultaneous enhancement of the gap-like feature and sub-band at intermediate thickness establishes a direct link between the layer-controlled electronic structure and electron−phonon-induced spectral renormalization. While previous experiments on another molecular system, rubrene, have identified the presence of a gap-like feature arising from electron−phonon coupling,[59] the systematic evolution of band renormalization with coupling strength has remained largely unexplored. Our results provide such a thickness-resolved perspective, revealing how electron−phonon coupling evolves across the crossover from the two-dimensional to three-dimensional limit.

More broadly, these findings may also shed light on quantum phenomena related to electron−phonon coupling in C_{60}, including the role of high-frequency intramolecular phonons in unconventional superconductivity.[24,60] Beyond the specific case of C_{60}, our results highlight molecular thin films as a versatile platform for engineering the electronic structure and many-body interactions. In addition to dimensionality, molecular orientation provides an additional tuning axis for intermolecular coupling, distinguishing molecular solids from conventional layered materials. In contrast to moiré-based approaches in van der Waals materials, where the interaction strength is tuned through the twist angle and heterostructure stacking, molecular systems offer a complementary route based on the layer number, molecular orientation, and substrate registry. This flexibility provides new opportunities for designing tunable quantum states in molecular solids using experimentally accessible structural parameters.

■ ASSOCIATED CONTENT

Supporting Information

The Supporting Information is available free of charge at https://pubs.acs.org/doi/10.1021/acs.nanolett.6c02272.

Downloaded from pubs.acs.org/naletd/article-pdf/26/37/12259/6839856/acs.nanolett.6c02272.pdf by CHINESE UNIV OF HONG KONG SHENZHEN user on 02 November 2026

https://doi.org/10.1021/acs.nanolett.6c02272
Nano Lett. 2026, 26, 12259−12267

Experimental and theoretical methods, including C_{60} film growth, high-resolution ARPES measurements, and TD-DMRG calculations of the single-particle spectral function with electron−phonon coupling; note on phonon-induced gap formation; background-subtracted EDC analysis; simulated spectral functions for different electron−phonon coupling distributions; and raw-intensity evidence for the weak sub-band feature in the 5 ML C_{60} film (PDF)

AUTHOR INFORMATION

Corresponding Author

Alessandra Lanzara − *Department of Physics and Kavli Energy NanoScience Institute, University of California, Berkeley, Berkeley, California 94720, United States; Materials Sciences Division, Lawrence Berkeley National Laboratory, Berkeley, California 94720, United States;* Email: alanzara@lbl.gov

Authors

Hai-Lan Luo − *Department of Physics, University of California, Berkeley, Berkeley, California 94720, United States; Materials Sciences Division, Lawrence Berkeley National Laboratory, Berkeley, California 94720, United States;* orcid.org/0000-0002-9925-0450

Weitang Li − *Guangdong Basic Research Center of Excellence for Aggregate Science, School of Science and Engineering, The Chinese University of Hong Kong, Shenzhen, Guangdong 518172, China*

Luca Moreschini − *Department of Physics, University of California, Berkeley, Berkeley, California 94720, United States; Materials Sciences Division, Lawrence Berkeley National Laboratory, Berkeley, California 94720, United States*

Jonathan Denlinger − *Advanced Light Source, Lawrence Berkeley National Laboratory, Berkeley, California 94720, United States*

Zhigang Shuai − *Guangdong Basic Research Center of Excellence for Aggregate Science, School of Science and Engineering, The Chinese University of Hong Kong, Shenzhen, Guangdong 518172, China; MOE Key Laboratory for Organic Optoelectronics and Molecular Engineering, Department of Chemistry, Tsinghua University, Beijing 100084, China;* orcid.org/0000-0003-3867-2331

Claudia Ojeda-Aristizabal − *Department of Physics and Astronomy, California State University, Long Beach, Long Beach, California 90840, United States;* orcid.org/0000-0003-0816-9727

Complete contact information is available at: https://pubs.acs.org/10.1021/acs.nanolett.6c02272

Author Contributions

A.L. conceived the project. J.D. and C.O.-A. contributed to the film growth and performed the ARPES experiments. H.-L.L. analyzed the ARPES data with help from L.M. W.L. and Z.S. contributed to the calculations. H.-L.L. and A.L. wrote the manuscript with input from all coauthors. All authors participated in discussions and commented on the manuscript.

Notes

The authors declare no competing financial interest.

ACKNOWLEDGMENTS

We thank Drew W. Latzke for experimental help and Jack Broad and Sinéad M. Griffin for helpful discussions. This work was primarily supported by the U.S. Department of Energy, Office of Science, Office of Basic Energy Sciences, Materials Sciences and Engineering Division, under Contract DE-AC02-05CH11231 within the van der Waals heterostructure Program (KCWF16). This research used resources of the Advanced Light Source, a U.S. DOE Office of Science User Facility, under Contract DE-AC02-05CH11231. C.O.-A. acknowledges the U.S. Department of Energy, Office of Science, Office of Basic Energy Sciences, under Award DE-SC0018154 for film growth and ARPES data acquisition.

REFERENCES

(1) Basov, D. N.; Averitt, R. D.; Hsieh, D. Towards properties on demand in quantum materials. *Nat. Mater.* **2017**, *16*, 1077−1088.

(2) Keimer, B.; Moore, J. E. The physics of quantum materials. *Nat. Phys.* **2017**, *13*, 1045−1055.

(3) Bistritzer, R.; MacDonald, A. H. Moiré bands in twisted double-layer graphene. *Proc. Natl. Acad. Sci. U. S. A.* **2011**, *108*, 12233−12237.

(4) Cao, Y.; Fatemi, V.; Demir, A.; Fang, S.; Tomarken, S. L.; Luo, J. Y.; Sanchez-Yamagishi, J. D.; Watanabe, K.; Taniguchi, T.; Kaxiras, E.; Ashoori, R. C.; Jarillo-Herrero, P. Correlated insulator behaviour at half-filling in magic-angle graphene superlattices. *Nature* **2018**, *556*, 80−84.

(5) Gunnarsson, O. Superconductivity in fullerides. *Rev. Mod. Phys.* **1997**, *69*, 575.

(6) Powell, B. J.; McKenzie, R. H. Quantum frustration in organic Mott insulators: from spin liquids to unconventional superconductors. *Rep. Prog. Phys.* **2011**, *74*, No. 056501.

(7) Jérome, D. Organic conductors: from charge density wave TTF-TCNQ to superconducting $(TMTSF)_2PF_6$. *Chem. Rev.* **2004**, *104*, 5565−5591.

(8) Nematiaram, T.; Padula, D.; Troisi, A. Bright Frenkel Excitons in Molecular Crystals: A Survey. *Chem. Mater.* **2021**, *33*, 3368−3378.

(9) Wang, Y.; Yamachika, R.; Wachowiak, A.; Grobis, M.; Crommie, M. F. Tuning fulleride electronic structure and molecular ordering via variable layer index. *Nat. Mater.* **2008**, *7*, 194−197.

(10) Brouet, V.; Yang, W. L.; Zhou, X. J.; Choi, H. J.; Louie, S. G.; Cohen, M. L.; Goldoni, A.; Parmigiani, F.; Hussain, Z.; Shen, Z. X. Orientation-Dependent C_{60} Electronic Structures Revealed by Photoemission Spectroscopy. *Phys. Rev. Lett.* **2004**, *93*, No. 197601.

(11) Yu, G.; Gao, J.; Hummelen, J. C.; Wudl, F.; Heeger, A. J. Polymer Photovoltaic Cells: Enhanced Efficiencies via a Network of Internal Donor-Acceptor Heterojunctions. *Science* **1995**, *270*, 1789−1791.

(12) Günes, S.; Neugebauer, H.; Sariciftci, N. S. Conjugated polymer-based organic solar cells. *Chem. Rev.* **2007**, *107*, 1324−1338.

(13) Li, H.; Tee, B. C.-K.; Cha, J. J.; Cui, Y.; Chung, J. W.; Lee, S. Y.; Bao, Z. High-mobility field-effect transistors from large-area solution-grown aligned C_{60} single crystals. *J. Am. Chem. Soc.* **2012**, *134*, 2760−2765.

(14) Wojciechowski, K.; Leijtens, T.; Siprova, S.; Schlueter, C.; Hörantner, M. T.; Wang, J. T.-W.; Li, C.-Z.; Jen, A. K.-Y.; Lee, T.-L.; Snaith, H. J. C_{60} as an Efficient n-Type Compact Layer in Perovskite Solar Cells. *J. Phys. Chem. Lett.* **2015**, *6*, 2399−2405.

(15) Ojeda-Aristizabal, C.; et al. Molecular Arrangement and Charge Transfer in C_{60}/Graphene Heterostructures. *ACS Nano* **2017**, *11*, 4686.

(16) Said, A. A.; et al. Sublimed C_{60} for efficient and repeatable perovskite-based solar cells. *Nat. Commun.* **2024**, *15*, 708.

(17) Heiney, P. A.; Fischer, J. E.; McGhie, A. R.; Romanow, W. J.; Denenstein, A. M.; McCauley, J. P., Jr.; Smith, A. B.; Cox, D. E. Orientational Ordering Transition in Solid C_{60}. *Phys. Rev. Lett.* **1991**, *66*, 2911.

https://doi.org/10.1021/acs.nanolett.6c02272
Nano Lett. 2026, 26, 12259−12267

Downloaded from pubs.acs.org/naletd/article-pdf/26/37/12259/6839856/acs.nanolett.6c02272.pdf by CHINESE UNIV OF HONG KONG SHENZHEN user on 02 November 2026

(18) Gugenberger, F.; Heid, R.; Meingast, C.; Adelmann, P.; Braun, M.; Wuhl, H.; Haluska, M.; Kuzmany, H. Glass transition in single-crystal C_{60} studied by high-resolution dilatometry. *Phys. Rev. Lett.* **1992**, *69*, 3774.
(19) Hebard, A. F.; Rosseinsky, M. J.; Haddon, R. C.; Murphy, D. W.; Glarum, S. H.; Palstra, T. T. M.; Ramirez, A. P.; Kortan, A. R. Superconductivity at 18 K in potassium-doped C_{60}. *Nature* **1991**, *350*, 600.
(20) Allemand, P.-M.; Khemani, K. C.; Koch, A.; Wudl, F.; Holczer, K.; Donovan, S.; Grüner, G.; Thompson, J. D. Organic Molecular Soft Ferromagnetism in a Fullerene C_{60}. *Science* **1991**, *253*, 301−302.
(21) Ganin, A. Y.; Takabayashi, Y.; Jeglic, P.; Arcon, D.; Potocnik, A.; Baker, P. J.; Ohishi, Y.; McDonald, M. T.; Tzirakis, M. D.; McLennan, A.; Darling, G. R.; Takata, M.; Rosseinsky, M. J.; Prassides, K. Polymorphism control of superconductivity and magnetism in Cs_3C_{60} close to the Mott transition. *Nature* **2010**, *466*, 221−225.
(22) Yang, W. L.; Brouet, V.; Zhou, X. J.; Choi, H. J.; Louie, S. G.; Cohen, M. L.; Kellar, S. A.; Bogdanov, P. V.; Lanzara, A.; Goldoni, A.; Parmigiani, F.; Hussain, Z.; Shen, Z.-X. Band Structure and Fermi Surface of Electron-Doped C_{60} Monolayers. *Science* **2003**, *300*, 303−307.
(23) Ganin, A. Y.; Takabayashi, Y.; Khimyak, Y. Z.; Margadonna, S.; Tamai, A.; Rosseinsky, M. J.; Prassides, K. Bulk superconductivity at 38 K in a molecular system. *Nat. Mater.* **2008**, *7*, 367−371.
(24) Zhou, J. S.; et al. Evidence for Band Renormalizations in Strong-Coupling Superconducting Alkali-Fulleride Films. *Phys. Rev. Lett.* **2023**, *130*, No. 216004.
(25) Ai, P.; Moreschini, L.; Mori, R.; Latzke, D. W.; Denlinger, J. D.; Zettl, A.; Ojeda-Aristizabal, C.; Lanzara, A. Linearly dispersive bands at the onset of correlations in K_xC_{60} films. *Phys. Rev. Res.* **2023**, *5*, L022042.
(26) McCann, E. Asymmetry gap in the electronic band structure of bilayer graphene. *Phys. Rev. B* **2006**, *74*, 161403.
(27) Partoens, B.; Peeters, F. M. From graphene to graphite: Electronic structure around the *K* point. *Phys. Rev. B* **2006**, *74*, No. 075404.
(28) Mak, K. F.; Sfeir, M. Y.; Misewich, J. A.; Heinz, T. F. The evolution of electronic structure in few-layer graphene revealed by optical spectroscopy. *Proc. Natl. Acad. Sci. U.S.A.* **2010**, *107*, 14999−15004.
(29) Ohta, T.; Bostwick, A.; McChesney, J. L.; Seyller, T.; Horn, K.; Rotenberg, E. Interlayer Interaction and Electronic Screening in Multilayer Graphene Investigated with Angle-Resolved Photoemission Spectroscopy. *Phys. Rev. Lett.* **2007**, *98*, No. 206802.
(30) Mak, K. F.; Lee, C.; Hone, J.; Shan, J.; Heinz, T. F. Atomically Thin MoS_2: A New Direct-Gap Semiconductor. *Phys. Rev. Lett.* **2010**, *105*, No. 136805.
(31) Splendiani, A.; Sun, L.; Zhang, Y.; Li, T.; Kim, J.; Chim, C.-Y.; Galli, G.; Wang, F. Emerging Photoluminescence in Monolayer MoS_2. *Nano Lett.* **2010**, *10*, 1271−1275.
(32) Zhang, Y.; et al. Direct observation of the transition from indirect to direct bandgap in atomically thin epitaxial $MoSe_2$. *Nat. Nanotechnol.* **2014**, *9*, 111−115.
(33) Gupta, A.; Sakthivel, T.; Seal, S. Recent development in 2D materials beyond graphene. *Prog. Mater. Sci.* **2015**, *73*, 44−126.
(34) Tjeng, L. H.; Hesper, R.; Heessels, A. C. L.; Heeres, A.; Jonkman, H. T.; Sawatzky, G. A. Development of the electronic structure in a K-doped C_{60} monolayer on a Ag(111) surface. *Solid State Commun.* **1997**, *103*, 31−35.
(35) Hou, J. G.; Jinlong, Y.; Haiqian, W.; Qunxiang, L.; Changgan, Z.; Lanfeng, Y.; Bing, W.; Chen, D. M.; Qingshi, Z. Topology of two-dimensional C_{60} domains. *Nature* **2001**, *409*, 304−305.
(36) Park, H.; Park, J.; Lim, A. K. L.; Anderson, E. H.; Alivisatos, A. P.; McEuen, P. L. Nanomechanical oscillations in a single-C_{60} transistor. *Nature* **2000**, *407*, 57−60.
(37) Latzke, D. W.; Ojeda-Aristizabal, C.; Griffin, S. M.; Denlinger, J. D.; Neaton, J. B.; Zettl, A.; Lanzara, A. Observation of highly dispersive bands in pure thin film C_{60}. *Phys. Rev. B* **2019**, *99*, No. 045425.
(38) Haag, N.; Lüftner, D.; Haag, F.; Seidel, J.; Kelly, L. L.; Zamborlini, G.; Jugovac, M.; Feyer, V.; Aeschlimann, M.; Puschnig, P.; Cinchetti, M.; Stadtmüller, B. Signatures of an atomic crystal in the band structure of a C_{60} thin film. *Phys. Rev. B* **2020**, *101*, No. 165422.
(39) Golden, M. S.; Knupfer, M.; Fink, J.; Armbruster, J. F.; Cummins, T. R.; Romberg, H. A.; Roth, M.; Sing, M.; Schmidt, M.; Sohmen, E. The electronic structure of fullerenes and fullerene compounds from high-energy spectroscopy. *J. Phys.: Condens. Matter* **1995**, *7*, 8219.
(40) Latzke, D. W.; Ojeda-Aristizabal, C.; Denlinger, J. D.; Reno, R.; Zettl, A.; Lanzara, A. Orbital Character Effects in the Photon Energy and Polarization Dependence of Pure C_{60} Photoemission. *ACS Nano* **2019**, *13*, 12710−12718.
(41) Kang, M.; Jung, S. W.; Shin, W. J.; Sohn, Y.; Ryu, S. H.; Kim, T. K.; Hoesch, M.; Kim, K. S. Holstein polaron in a valley-degenerate two-dimensional semiconductor. *Nat. Mater.* **2018**, *17*, 676−680.
(42) Chen, C.; Avila, J.; Wang, S.; Wang, Y.; Mucha-Kruczynski, M.; Shen, C.; Yang, R.; Nosarzewski, B.; Devereaux, T. P.; Zhang, G.; Asensio, M. C. Emergence of Interfacial Polarons from Electron-Phonon Coupling in Graphene/h-BN van der Waals Heterostructures. *Nano Lett.* **2018**, *18*, 1082−1087.
(43) Lee, J. J.; Schmitt, F. T.; Moore, R. G.; Johnston, S.; Cui, Y.-T.; Li, W.; Yi, M.; Liu, Z. K.; Hashimoto, M.; Zhang, Y.; Lu, D. H.; Devereaux, T. P.; Lee, D.-H.; Shen, Z.-X. Interfacial mode coupling as the origin of the enhancement of *Tc* in FeSe films on $SrTiO_3$. *Nature* **2014**, *515*, 245.
(44) Goodvin, G. L.; Berciu, M.; Sawatzky, G. A. Green's function of the Holstein polaron. *Phys. Rev. B* **2006**, *74*, No. 245104.
(45) Satoshi, K.; Hiroyuki, Y.; Nobuo, U.; Kera, S; Yamane, H.; Ueno, N. First-principles measurements of charge mobility in organic semiconductors: Valence hole−vibration coupling in organic ultrathin films. *Prog. Surf. Sci.* **2009**, *84*, 135−154.
(46) Ciuchi, S.; Fratini, S. Band Dispersion and Electronic Lifetimes in Crystalline Organic Semiconductors. *Phys. Rev. Lett.* **2011**, *106*, No. 166403.
(47) Li, W.; Ren, J.; Shuai, Z. A general charge transport picture for organic semiconductors with nonlocal electron-phonon couplings. *Nat. Commun.* **2021**, *12*, 4260.
(48) Gunnarsson, O.; Handschuh, H.; Bechthold, P. S.; Kessler, B.; Ganteför, G.; Eberhardt, W. Photoemission Spectra of C_{60}^-: Electron-Phonon Coupling, Jahn-Teller Effect and Superconductivity in the Fullerides. *Phys. Rev. Lett.* **1995**, *74*, 1875.
(49) Huang, Z.; Liu, D. First principles study of the vibronic coupling in positively charged C_{60}^+. *Chem. Phys. Lett.* **2020**, *754*, No. 137698.
(50) Nigam, A.; Schwabegger, G.; Ullah, M.; Ahmed, R.; Fishchuk, I. I.; Kadashchuk, A.; Simbrunner, C.; Sitter, H.; Premaratne, M.; Ramgopal Rao, V. Strain induced anisotropic effect on electron mobility in C_{60} based organic field effect transistors. *Appl. Phys. Lett.* **2012**, *101*, No. 083305.
(51) Bakulin, A. A.; Lovrincic, R.; Yu, X.; Selig, O.; Bakker, H. J.; Rezus, Y. L.; Nayak, P. K.; Fonari, A.; Coropceanu, V.; Brédas, J.-L.; Cahen, D. Mode-selective vibrational modulation of charge transport in organic electronic devices. *Nat. Commun.* **2015**, *6*, 7880.
(52) Kubo, T.; Häusermann, R.; Tsurumi, J.; Soeda, J.; Okada, Y.; Yamashita, Y.; Akamatsu, N.; Shishido, A.; Mitsui, C.; Okamoto, T.; Yanagisawa, S.; Matsui, H.; Takeya, J. Suppressing molecular vibrations in organic semiconductors by inducing strain. *Nat. Commun.* **2016**, *7*, 11156.
(53) Mann, C.; West, D.; Miotkowski, I.; Chen, Y. P.; Zhang, S.; Shih, C.-K. Mapping the 3D surface potential in Bi_2Se_3. *Nat. Commun.* **2013**, *4*, 2277.
(54) Kalb, W. L.; Haas, S.; Krellner, C.; Mathis, T.; Batlogg, B. Trap density of states in small-molecule organic semiconductors: A quantitative comparison of thin-film transistors with single crystals. *Phys. Rev. B* **2010**, *81*, No. 155315.

Downloaded from pubs.acs.org/naletd/article-pdf/26/37/12259/6394856/acs.nanolett.6c02272.pdf by CHINESE UNIV OF HONG KONG SHENZHEN user on 02 November 2026

https://doi.org/10.1021/acs.nanolett.6c02272
Nano Lett. 2026, 26, 12259−12267

(55) Si, C.; Liu, Z.; Duan, W.; Liu, F. First-Principles Calculations on the Effect of Doping and Biaxial Tensile Strain on Electron-Phonon Coupling in Graphene. *Phys. Rev. Lett.* **2013**, *111*, No. 196802.
(56) He, J.; Zhu, X.; Liu, W.; Hu, E.; Wang, J.; Zhang, R. Versatile band structure and electron-phonon coupling in layered $PtSe_2$ with strong interlayer interaction. *Nano Research* **2022**, *15*, 6613−6619.
(57) Ohno, K.; Kawazoe, Y. Abnormal intermolecular interaction between overlayer C_{60} molecules due to induced dipole moments in C_{60} thin films adsorbed on substrates. *Scripta Materialia* **2001**, *44*, 1579−1582.
(58) Pandeya, R. P.; Shchukin, K. P.; Falke, Y.; Mussler, G.; Jalil, A. R.; Atodiresei, N.; Hasdeo, E. H.; Fedorov, A.; Senkovskiy, B. V.; Jansen, D.; Di Santo, G.; Petaccia, L.; Gruneis, A. Molecular order induced charge transfer in a C_{60}-topological insulator moiré heterostructure. *Nano Lett.* **2025**, *25*, 1220−1225.
(59) Bussolotti, F.; Yang, J.; Yamaguchi, T.; Yonezawa, K.; Sato, K.; Matsunami, M.; Tanaka, K.; Nakayama, Y.; Ishii, H.; Ueno, N.; Kera, S. Hole-phonon coupling effect on the band dispersion of organic molecular semiconductors. *Nat. Commun.* **2017**, *8*, 173.
(60) Dresselhaus, M. S.; Dresselhaus, G.; Eklund, P. C. *Science of Fullerenes and Carbon Nanotubes: Their Properties and Applications*; Elsevier Science: Amsterdam, The Netherlands, 1996; Chapter 15.

Downloaded from pubs.acs.org/naletd/article-pdf/26/37/12259/6839486/acs.nanolett.6c02272.pdf by CHINESE UNIV OF HONG KONG SHENZHEN user on 02 November 2026

https://doi.org/10.1021/acs.nanolett.6c02272
Nano Lett. 2026, 26, 12259−12267